A feasibility study of a rotary planar electrode array for electrical impedance mammography using a digital breast phantom

X Zhang[1], C Chatwin[1], D C Barber[2]

1. Department of Engineering, University of Sussex, Brighton BN1 9QT, UK
2. Department of Cardiovascular Science, University of Sheffield, Sheffield, S1 4DT, UK

E-mail: xz68@sussex.ac.uk

Abstract

A feasibility study of an electrical impedance mammography (EIM) system with a rotary planar electrode array, named RPEIM, is presented. The RPEIM system is an evolution of the Sussex MK4 system, which is a prototype instrument for breast cancer detection. Comparing it with the other planar electrode EIM systems, the rotation feature enables a dramatic increase in the number of independent measurements. To assist impedance evaluation exploiting electrode array rotation, a synchronous mesh method is proposed. Using the synchronous mesh method, the RPEIM system is shown to have superior performance in image accuracy, spatial resolution and noise tolerance over the MK4 system. To validate the study, we report simulations based on a close-to-realistic 3D digital breast phantom, which comprises of: skin, nipple, ducts, acinus, fat and tumor. A digital breast phantom of a real patient is constructed, whose tumor was detected using the MK4 system. The reconstructed conductivity image of the breast phantom indicates that the breast phantom is a close replica of the patient's real breast as assessed by the MK4 system in a clinical trial. A comparison between the RPEIM system and the MK4 system is made based on this phantom to assess the advantages of the RPEIM system.

Keywords: breast cancer detection, breast phantom, electrical impedance mammography, electrical impedance tomography

1. Introduction

Electrical Impedance Mammography (EIM) is a medical imaging modality for investigating the internal conductivity or/and permittivity distribution of a breast. According to the studies on the freshly excised human breast tissue, typically, the malignant tumor has a much higher conductivity and permittivity than the surrounding normal tissue (Campbell and Land, 1992, Hassan and El-Shenawee, 2011, Jossinet, 1996, Jossinet, 1998, Lazebnik et al., 2007, Guofeng et al., 2012, Surowiec et al., 1988), thus an area with abnormally high conductivity

or/and permittivity in the reconstructed image may be an indicator of breast cancer. However it is very challenging to accurately reconstruct the unknown conductivity or/and permittivity from a modest number of surface measurements, as it is a very ill-posed problem. In practice, the performances of the ill-posed problem is made difficult by: 1) the changes of the surface measurements, which are caused by a big tumor with a considerable high conductivity, may be undetectable at the required precision; 2) although the changes of the surface measurements are detectable at the given precision, the volume of the tumor in the reconstructed image is much bigger than the real size or/and there are false positives in the reconstructed image, which may be caused by noise or other factors. To solve the EIM problem, a breast is numerically approximated by a finite number of elements in the 3D domain. The element at a particular position with the corresponding value of conductivity or/and permittivity is chosen as the unknown (degree of freedom). For a chosen discretization of a breast, if ignoring the noise in the measurements, the number of degrees of freedom of this system is determined by the number of the independent measurements. More independent measurements provide more constraints to the field, which will decrease the number of degrees of freedom of the unknowns and hence is beneficial to the solution stability. Typically, increasing the number of electrodes is the most straightforward method to increase the number of independent measurements, however electrodes cannot be deployed in an unlimited manner due to their physical size; therefore flexible electrode arrays were studied aiming to increase independent measurements with a limited number of electrodes.

Frounchi and Bazzazi (2003) developed a novel rotary electrical capacitance tomography (ECT) system with 4 electrodes evenly deployed in a ring (Frounchi and Bazzazi, 2003). The circular electrode array rotates through 90 degrees and for each rotation, 6 measurements are collected. According to their report, the rotation of the electrode array contributed to a dramatic increase in the number of independent measurements and thus achieved fairly high resolution images. Murphy and York (2006) proposed using non-stationary electrodes to monitor a mixing process, by fixing the electrodes onto the mixing impeller (Murphy and York, 2006). According to their simulations, the employment of the non-stationary electrodes, in an electrical impedance tomography (EIT) system, increases the number of the independent observations; as a result there are significant improvements in the resolution, the information content and the reliability of the reconstructed image. Huang, Yu and Chung (2007) reported a movable ring electrode array in their EIT system, named REIT (Yu et al., 2006, Huang et al., 2007). The REIT is equipped with 16 evenly distributed electrodes fixed on a ring rotational frame with a minimum and maximum rotation angle of 0.018 and 22.5 degrees respectively. This design allowed up to 1250 groups of measurements and produced a maximum of 130,000 independent measurements; however in practice, they only collected measurements from 5 positions due to the impractical length of time required for both data acquisition and image reconstruction. To support this rotating design, a finer mesh is required to make sure that every electrode is located at a mesh element.

Till now, only a few studies on rotary ring electrode array have been reported; the study of a movable planar electrode array is not available in the literature. The application of a moveable electrode array to EIT has not been widely studied as the following two problems are not solved: 1) the movement of the electrodes will perturb the field under investigation. In most EIT systems, electrodes are directly attached to the surface of the objects being

measured. The movement of the electrodes may affect the conductivity or/and permittivity distribution of the field, as a result, the boundary measurements from a movable electrode system may be sampled on several different fields, thus it would be inappropriate to use all these measurements to reconstruct one field. For example, in mastopathy diagnosis, the movements of electrodes may twist or change the shape or position of the breast. Even though the changes are small, considering the ill-posed nature of the EIT inverse problem, the results will be extremely unreliable; 2) a moveable electrode array relies on a much finer discretization, which not only increases computational time but also may worsen the ill-posed problem. In the EIT inverse problem, the electrodes are modeled by the mesh nodes or mesh elements at the corresponding positions. As the electrodes rotate, to record data from different positions, the measuring density (or the positions of the electrodes) will increase. To ensure that all the measuring electrodes are modeled by proper mesh nodes or mesh elements, the traditional method is to use a finer mesh, thus the more movements the electrode array makes, the finer the mesh is. However, studies suggest that a significantly finer mesh, whose elements are far smaller than the size that the system can distinguish, will result in greater ill-conditioning (Gisser et al., 1990, Tang et al., 2002). Thus, using a moveable electrode array in the EIT systems needs to: 1) prevent the disturbances from the moveable electrode array to the field under investigation; 2) avoid using an unreasonably fine mesh to support the movements of the electrode array in image reconstruction.

We plan to update our 3D EIM system, the Sussex MK4 system (Zhang et al., 2014d, Sze, 2012), by using a rotary planar electrode array, as this will enhance the resolution; however before manufacturing new equipment, sufficient and comprehensive simulations are necessary to analyze the advantages of the new design. This will forecast how much improvement we can achieve, so that we can determine if the new equipment is worth investing in. The aims of this paper are: 1) providing methods to apply the rotary planar electrode array to the EIM system for breast cancer detection; 2) proving that the rotary planar electrode array EIM (RPEIM) system will contribute to better accuracy, resolution, and noise tolerance. To assess the performance of EIT systems, many phantoms were studied (Gagnon et al., 2010, Holder et al., 1996, Sadleir et al., 2013). In this paper, we propose a close-to-realistic digital breast phantom. This paper is organized as follows. Section 2 introduces the implementation of the RPEIM system, which includes the design of the RPEIM system, the method to build the breast phantoms, and the solutions of the forward and inverse problem. Section 3 demonstrates the improvements of the RPEIM system over the MK4 system. The discussion of this new system is given in Section V. Section VI concludes this paper and outlines the prospects for future work.

2. Method

2.1 A brief introduction of the RPEIM system

The achievement of the Sussex MK4 system based on phantoms and the real patients made us believe that using EIT to detect breast cancer is realistic (Zhang et al., 2014d, Sze, 2012); however we are also aware of the limited ability of the MK4 system in image resolution and reliability. The RPEIM system is an upgraded version of the Sussex MK4 system, which aims

to enhance the performance of our EIM system. The appearance of the RPEIM system is the same as the MK4 system, which is a bed with a data acquisition tank in the appropriate position. The data acquisition tank is comprised of a support tank, a breast container and an adjustable scanner head, which is shown in Figure 1. The support tank is used to support and fasten the breast container to prevent its movement. The breast container is replaceable and has different sizes to accommodate different brassiere cups. The differently sized breast containers have the same diameter, which is 18cm but varying depths, which are 1 cm, 1.5 cm, 2 cm, and up to 5 cm. The wall of the breast container is made from non-conducting material (Figure 1 in green). The bottom of the breast container is 3mm thick and made from conducting material with a conductivity of approximately 0.05 S/m (Figure 1 in blue). The scanner head is a planar electrode array. It is adjustable in the vertical direction and rotatable in the horizontal plane. The rotation range is from 0° to 60°. The RPEIM system retains the design of the hexagonal electrode arrangement and the data acquisition method of the MK4 system. The current excitations and voltage measurements are achieved in small hexagonal measurement areas. The total number of voltage measurements is 1416. For a detailed description of the hexagonal planar electrode array and the data acquisition method, please refer to (Sze, 2012, Zhang et al., 2014c). The improvement of the RPEIM system is that the rotation of the planar electrode array will significantly increase the number of the independent measurements. The examination process is: 1) choose an appropriately sized breast container for the patient; 2) fill the breast container with the body-temperature saline with a conductivity of 0.05 S/m; 3) the patient lies on the bed with a breast in the container; 4) raise up the scanner head to engage the electrodes with the bottom of the container and acquire a group of measurements; 5) move the scanner head to the start position; 6) rotate one degree, and return the scanner head to the measurement position and collect another group of measurements, 7) repeat 5) and 6) until sampling is finished. The employment of the breast container avoids breast movements during examinations as the scanner head rotates, so that all the measurements correspond to the same conductivity distribution. The planar electrode array rotates within a 60° segment. Normally equal angular sample is adopted; thus if N groups of measurements are required in the 60° segment, the electrode array will sample at $(p-1)*60/N,\ p=[1,2,\cdots,N]$. Returning the electrode array to the start position before making the next measurement will avoid accumulation of the rotation errors. For example, if we want 3 measurement positions at 0°, 20° and 40°, for the last measurement position, the electrode array goes from 0° to 40° rather than 20° to 40°. This will avoid the rotation error at 20°.

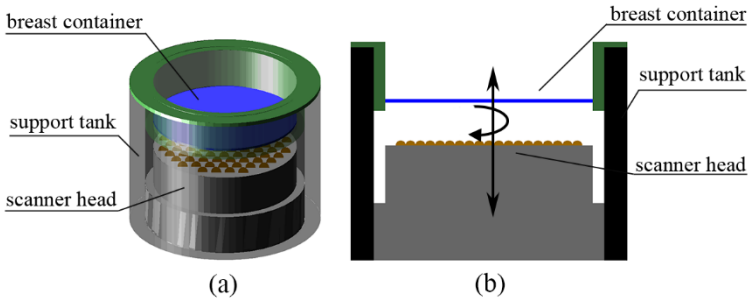

Figure 1. The data acquisition tank. (a) is a 3D view of the tank with the electrodes in the lowered position. (b) is the vertical cross-section of the tank

2.2 The traditional method and the synchronous mesh method for the rotary-electrode EIT system.

In the former EIT system, the traditional method to support the rotation of the electrode array is subdividing the mesh in the area near the electrodes. This is an effective method for the rotary ring electrode array, as normally the number of the electrodes of the circular array is small and the mesh in use is 2D, so the number of mesh elements won't be too huge (for example Figure 6 in reference (Yu et al., 2006)). However the traditional method is not suitable for the RPEIM system for the following reasons:

(1) Using the traditional method will significantly increase the data volume and the computational time. Figure 2 (a) shows the 2D mesh for the static detection, where the 85 red dots indicate the positions of the electrodes of the planar electrode array. Figure 2 (b) shows the the subdivided mesh to support the rotations of the planar electrode array, where the dots in different color indicate different measurement positions of the planar electrode array. The 2D mesh in Figure 2 (a) has 421 nodes and 780 elements; for 3D imaging, the numbers of the 3D mesh nodes and elements are $421 \times (L+1)$ and $780 \times 3 \times L$, where L indicates the number of layers of the 3D mesh. The 2D mesh in Figure 2 (b) has 673 nodes and 1284 elements; for 3D imaging, the numbers of the 3D mesh nodes and elements are $673 \times (L+1)$ and $1284 \times 3 \times L$. Obviously using the subdivided mesh will result in a significant increase in the data volume and hence the computational time.

(2) Using the traditional method will worsen the ill-posed problem. As we mentioned before, if the elements are far smaller than the size that the system can distinguish, it will lead to greater ill-conditioning. Obviously there are many small sized elements in Figure 2 (b).

(3) Using the traditional method will increase the computational error. The ideal element for the finite element method (FEM) is the regular triangle (for the 3D problem, it is regular tetrahedron). Conversely, if the elements are far from the regular triangle/ tetrahedron, it will cause great computational error; however there are many elements in Figure 2 (b) which are far from the regular triangle.

(4) The sizes of the elements in Figure 2 (b) vary over a large range. This will cause nonuniform resolution of the reconstructed conductivity maps.

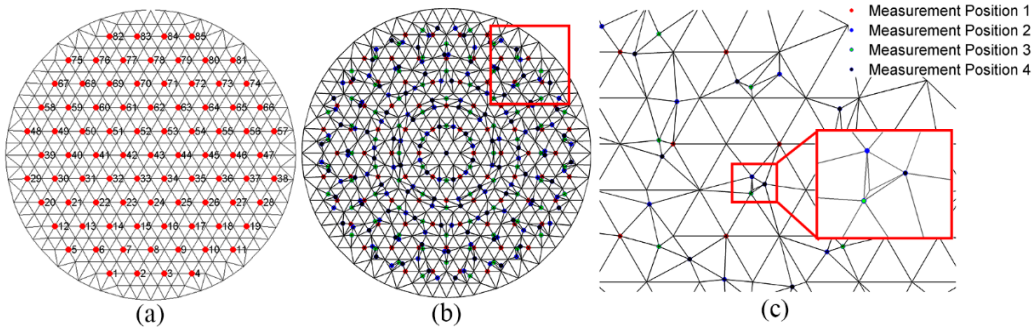

Figure 2. The meshes for the RPEIM system using the traditional method. (a) is the mesh for 1 measurement position. (b) is the mesh for 4 measurement positions. (c) is the amplification of the area highlighted by the red frame in (b). The spots indicate the positions of the electrodes.

The problems above will become worse as the number of measurement positions increases. We propose a synchronous mesh method, which is facilitated by rotating the mesh together with the electrodes, so that the electrodes can always locate at the same mesh nodes

or mesh elements. In the RPEIM system, we still use the point electrode model (PEM), which was used in the MK4 system (Zhang et al., 2014d). The synchronous mesh method for the RPEM system is shown in Figure 3. Figure 3 (a) indicates that the mesh and the electrodes at the original position 0°; Figure 3 (b) indicates that the electrodes have rotated 30° and the mesh rotates together with the electrodes 30°. The 19 highlighted dots in Figure 3 (a) and (b) indicate the same electrodes but at a different measurement position. The two big dots with '+', '-' indicate the current excitation electrodes. The 17 middle sized dots indicate the measuring electrodes, in which 12 voltage measurements are collected from the adjacent electrodes, parallel to the drive pair. The other small dots indicate the electrodes not participating in the data acquisition in this hexagonal measurement area. Figure 3 only presents one excitation event and its corresponding measurements; to understand the method that the hexagonal measurement area scans the whole filed, please refer to reference (Zhang et al., 2014d) and (Sze, 2012). By using the synchronous mesh method, the number of meshes in use is equal to the number of measurement positions.

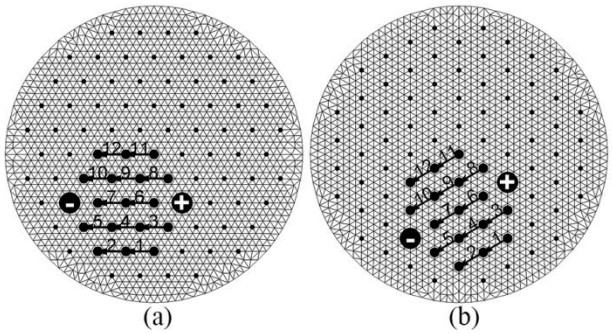

Figure 3. Two positions of the fine mesh, the planar electrode array and a hexagonal measurement area. (a) is the display of the original position. (b) is the display of the rotated position at 30°.

2.3 The forward problem

In the numerical modeling of the forward problem, we set up phantoms using analytic geometry first and then use a mesh to discretize it. The conductivity values of the mesh elements are equal to the conductivity at their centers. A close-to-real digital breast phantom is created in Figure 4, which is composed of skin, fat, ducts, acinus, gland area, a nipple and a tumor. This breast phantom is approximately 530 ml corresponding to a brassiere size of 34C. The breast container is 3cm in depth. The maximum diameter of the breast is 15cm. The diameter of the contact area between the breast and the bottom of the breast container is 9cm. The breast skin is 1.55 mm in thickness (Sutradhar and Miller, 2013) and the conductivity value is assumed to be 0.465 S/m (De Lucia et al., 2007). Normally, there are 14 to 18 lactiferous lobes converging to the nipple in an adult breast. Each lactiferous lobe follows a tree branching pattern, with the terminal ducts connecting with the acinus (The breast Anatomy, 2013). Thus in the phantom, a network of cylinders, arranged in a tree shape, is used to simulate the ducts (Figure 4 (e)) and a cluster of spheres at the end of the ducts is used to simulate the acini (Figure 4 (c)). The diameters of the major ducts (the first generation ducts developing from the nipple) have random values between 2.0 and 4.5 mm (Dähnert, 2007); the lengths of the major ducts have random values from 6.0 to 8.0 mm. The number of

the branches is a random value from 3 to 5. The lengths and the diameters of the ducts randomly decrease in the next generation as the ducts branch. At the ends of the last generation, the acini are connected with them. The nipple is a cylinder with a diameter of 10 mm and a projection of 10 mm (Hussain et al., 2003). The ducts, the acini and the nipple compose the mammary gland; they are assigned a conductivity value of 0.35 S/m (Jossinet, 1998, Lazebnik et al., 2007, Surowiec et al., 1988). The tissue around the mammary gland, named gland area (Figure 4 (c)), is more conductive than the adipose tissue but less conductive than the mammary gland; therefore it is given a conductivity of 0.2 S/m. An ellipsoid is randomly placed on a duct to represent a ductal carcinoma (tumor), it has a conductivity of 1 S/m (Campbell and Land, 1992). The size of the tumor is 2 cm in length, 1.5 cm in width and 1 cm in height; the center of the tumor is [2.5, 0, 1.5] cm. The other part of the breast is adipose tissue with a conductivity of 0.05 S/m. The conductivity of the saline is 0.05 S/m. The bottom of the breast container is 3 mm thick with a conductivity of 0.05 S/m.

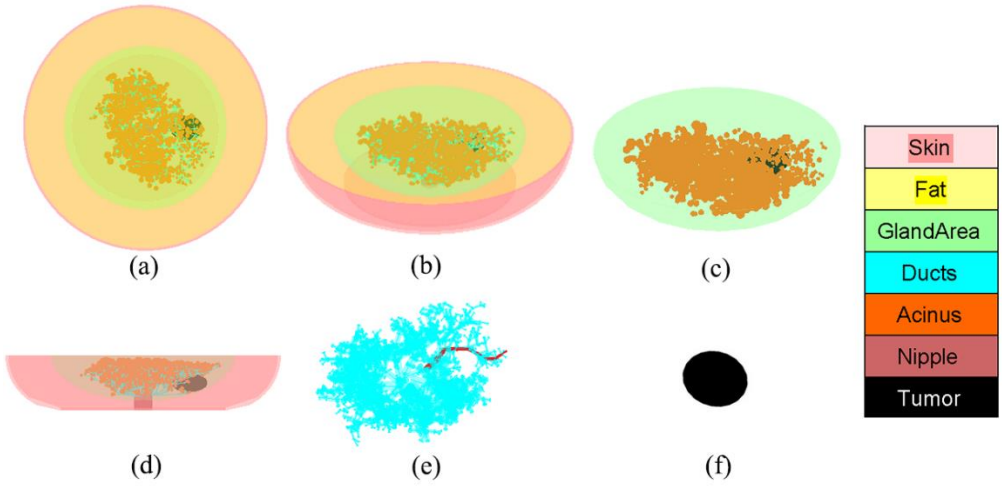

Figure 4. The analytic geometry model of a cancerous breast phantom. (a), (b), (d) are the XY view, the 3D view and the XZ view of the breast phantom. (c) shows the acinus, the tumor and the gland area. (e) shows the ducts, in which the red trace illustrates one route of the ducts. (f) is the tumor.

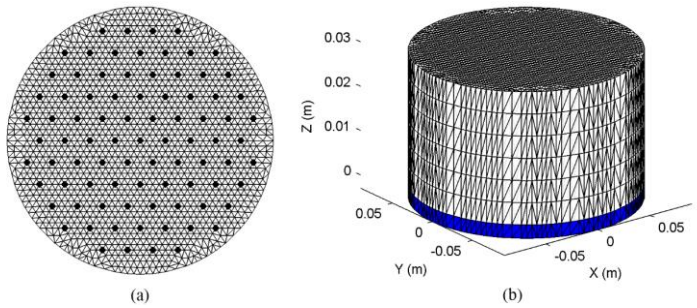

Figure 5. Meshes in the forward problem. (a) is the 2D fine mesh with the electrode arrangement. (b) is the 3D fine mesh applied to the forward problem.

The mesh, used to discretize the field in the breast container, is shown in Figure 5, it has 7 layers, 65,520 elements and 12,968 nodes. The bottom layer has 9,360 elements with a height of 3mm and conductivity of 0.05 S/m indicating the discretized bottom of the breast container. The other 6 layers are 5mm in height and have 56,160 elements in total, which are

used to discretize the field within the breast container including the breast phantom and the background saline. If the conductivity distribution in the breast container is $\sigma(x,y,z)$, the conductivity values of the mesh elements are

$$\sigma_i^p = \sigma\left(x_{i0}^p, y_{i0}^p, z_{i0}^p\right) \quad (1)$$

where σ_i^p indicates the conductivity value of the *i*th element of the *p*th mesh for the *p*th measurement position, $\left(x_{i0}^p, y_{i0}^p, z_{i0}^p\right)$ indicate the coordinate of the center of the *i*th element of the *p*th mesh. The discretized breast phantom corresponding to the original mesh and the 30°-rotation mesh are shown in Figure 6. We suggest using parallel computation to find the conductivity value of each element, as the computational time is very large. The breast phantom in Figure 4 is a small model with only about 4000 structures; however it requires at least 2.5 hours to work out the values of the elements for 4 measurement positions, using 20 i7[cc1] cores.

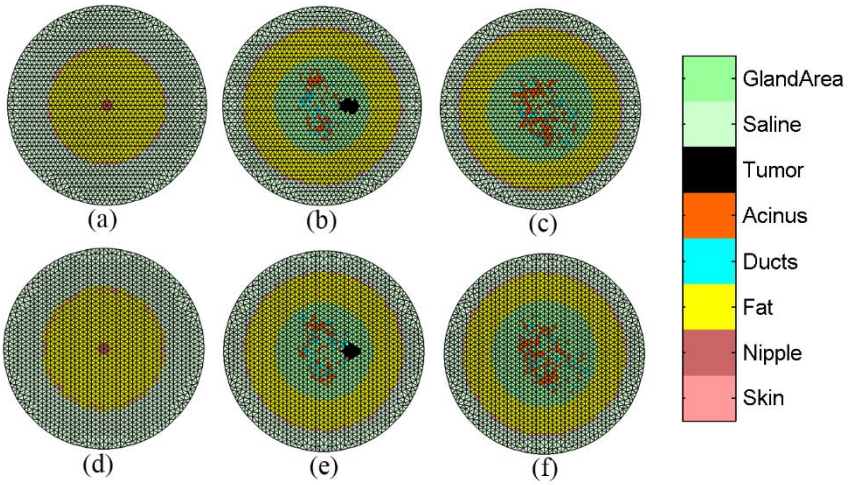

Figure 6. The discretized breast ohantom. (a) to (c) show the cross-sectional images of layer 1, 3, 5 in the mesh at the start position. (d) to (f) show the cross-sectional images of layer 1, 3, 5 in the mesh at the 30° position.

Knowing the conductivity values of the meshes, we can compute the voltage measurements. Assuming that there are *E* elements and *N* nodes in the mesh of the forward problem, the relationship between the current excitation and potential distribution is given by (2) (Dong et al., 2005, Xu et al., 2005, Babaeizadeh et al., 2006).

$$\phi = \left[Y(\sigma,x,y,z)\right]^{-1} Q \quad (2)$$

where Y is the forward solver, which is a sparse $N \times N$ matrix determined by the vertex coordinates and the conductivity values of the mesh elements, ϕ is the $N \times 1$ vector denoting the unknown nodal potential, $\phi = [\phi_1; \phi_2; \cdots; \phi_N]$, Q is the $N \times 1$ vector denoting the known nodal current, $Q = [Q_1; Q_1; \cdots; Q_N]$. If the current is excited between the *p*th and the *q*th nodes,

$$Q_n = \begin{cases} C & n = p \\ -C & n = q \\ 0 & otherwise \end{cases} \quad (3)$$

where Q_n denotes the *n*th element of Q, $n=[1,2,\cdots,N]$, C is a scalar equal to the current amplitude. For a direct-current supply, C is a constant; otherwise it is a function of time $C(t)$. The voltage measurements between the *j*th and the *h*th node are

$$V_{jh}^{pq}=\phi_h^{pq}-\phi_j^{pq} \quad (4)$$

where V_{jh}^{pq} indicate the voltage measurements between the *j*th and the *h*th node under the excitation between the *p*th and *q*th node, ϕ_h^{pq} and ϕ_j^{pq} indicate the potential at node *h* and *j*, under the excitation at node *p* and *q*. By using (1) to (4), we can evaluate the simulated voltage measurements.

In this simulation, we collect voltage measurements from 4 measurement positions. The operating frequency is 500 kHz, the sampling frequency is 20 MSa/s, the sample number is 1000, and the ADCs are 14 bit. We also assume that the background noise is 60dB white Gaussian noise; the multiplicative noise, which is caused by the amplifying circuit, is $\pm 0.5\%$ random noise. The ADC quantization is considered. The noise is added as shown in Figure 7, where Vi(tn) indicates the sample sequence of the *i*th measurement, Vi indicates the effective value of the sample sequence, which is the final measurement. For 1000 samples, the signal to noise ratio (SNR) of the whole system will be greater than 70 dB. Finally we get four groups of measurements at 0°, 15°, 30° and 45°, denoted by V^1, V^2, V^3, and V^4.

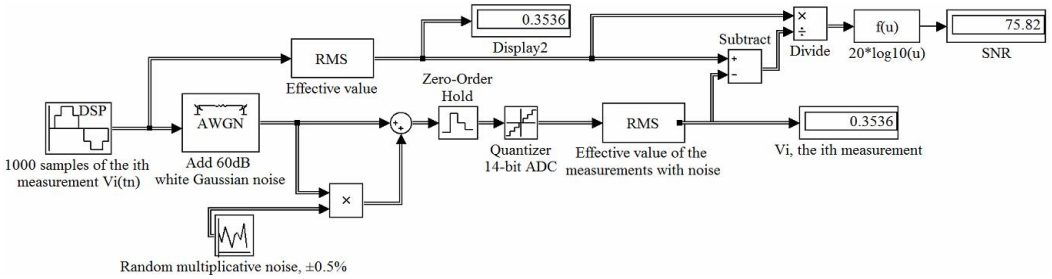

Figure 7. The addition of noise to the simulated measurements

2.4 The inverse problem

In the EIT inverse problem, the boundary measurements are known; the conductivity values of the mesh elements are the underdetermined parameters. To save computational time and avoid exacerbating the ill-conditioned problem, a coarse mesh with 4 layers, 14040 elements and 2947 nodes is used, shown in Figure 8. The height of the bottom layer is 3 mm indicating the bottom of the breast container; the heights of the other 3 layers are 10 mm.

We refer to the Sheffield algorithm, using the logarithm of the voltage ratios rather than the voltage differences to do the image reconstruction. Assuming that there are E_c elements and N_c nodes in the coarse mesh and M boundary measurements for one measurement position, the iterative image reconstruction algorithm is (5). For detailed information of this image reconstruction algorithm, please refer to reference (Sze, 2012, Barber, 2005, Zhang et al., 2014a, Zhang et al., 2014b).

$$\begin{cases} \Delta \ln \sigma = \left(F^T F + \alpha^2 I\right)^{-1}\left[F^T \ln\left(\dfrac{V}{V_n}\right) - \alpha^2 I \ln\left(\dfrac{\sigma_n}{\sigma_{ref}}\right)\right] \\ \ln \sigma_{n+1} = \ln \sigma_n + \Delta \ln \sigma \quad or \quad \sigma_{n+1} = \sigma_n e^{\Delta \ln \sigma} \end{cases} \tag{5}$$

where: F is the $M \times E_c$ sensitivity matrix, which is determined by the coordinates of the mesh nodes and the conductivity values of the mesh elements, α is the regularization parameter, which can be determined using the L-curve method (Hansen and Oleary, 1993, Vogel, 1996, Kaufman and Neumaier, 1996, Lavarello et al., 2006), I is the unit matrix, σ_{ref} is a $E_c \times 1$ vector indicating the reference conductivity distribution, which normally is a uniform field. In our case, the reference medium is saline and the conductivity is 0.05 S/m. V is the $M \times 1$ vectors indicating the real measurements. V_n indicates the *n*th predicted or simulated voltage measurements corresponding to the reconstructed conductivities σ_n. In the real experiment, $\ln(V/V_n)$ in (5) is replaced by

$$\ln\left(\frac{V}{V_n}\right) = \ln\left(\frac{V}{V_{ref}} * \frac{V_{sim\_ref}}{V_n}\right) = \ln\left(\frac{V}{V_{ref}}\right) - \ln\left(\frac{V_n}{V_{sim\_ref}}\right) \tag{6}$$

where: V_{ref} denotes the real reference measurements from the saline, V_{sim_ref} denotes the simulated reference measurements. Equation (6) will make sure that the real measurements and the simulated measurements could be compared separately, so that it will avoid the error caused by computer modelling. However in this paper, V is evaluated by simulations, so (5) is the equation we need.

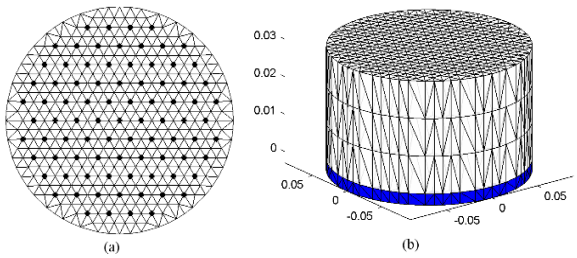

Figure 8. Meshes in the inverse problem. (a) is the 2D coarse mesh with the electrode arrangement. (b) is the 3D coarse mesh applied to the inverse problem.

The synchronous mesh requires different subdivisions of the field in the tank, which means if there are *N* groups of measurements, *N* 3D meshes corresponding to the *N* measurement positions will be needed. One group of measurements can only contribute to one group of solutions of the corresponding mesh. However in practice, we hope that all the groups of the measurements could interact with each other and finally achieve one 3D map, which is expected to be much better than any result from a single group of measurements. We propose the following steps to solve this problem: 1) make *N* 3D fine meshes for the forward problem and *N* 3D coarse meshes for the inverse problem; 2) solve the forward problems with some assumed conductivity and get *N* groups of predicted voltage measurements; 3) obtain the *N* groups of conductivity values (corresponding to coarse meshes) by using the image reconstruction algorithm; 4) map the conductivity values from the *N* 3D coarse meshes to the *N* 3D fine meshes (the mapping algorithm is shown in (7)); 5) if the conductivity distribution is

satisfied, make the *N* groups of conductivity a 3D image or a group of cross-sectional images; however if the conductivity distribution is not satisfied, repeat 2) to 5).

To introduce the synchronous mesh method in the inverse problem, we still use the breast phantom in Figure 4 as an example. Applying the four groups of measurements V^1, V^2, V^3, and V^4 to (5), the corresponding conductivity values $\sigma^1_{coarse\_1}$, $\sigma^2_{coarse\_1}$, $\sigma^3_{coarse\_1}$, and $\sigma^4_{coarse\_1}$ are computed, where '*coarse*' indicates the coarse mesh, 1 in the subscript indicates the first iteration, 1-4 in the superscript indicate the indexes of the measurement positions. $\sigma^1_{coarse\_1}$ and $\sigma^3_{coarse\_1}$ are visualized in Figure 9.

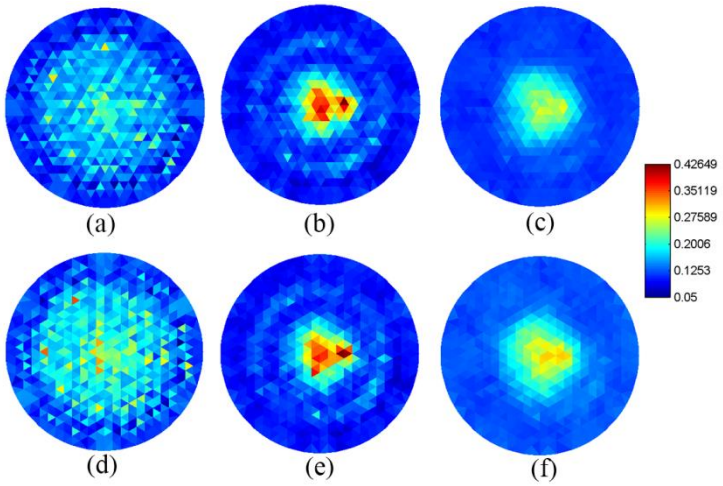

Figure 9. The reconstructed conductivity of the first iteration. (a) to (c) show the reconstructed conductivity at the first measurement position (0°). (d) to (f) show the reconstructed conductivity at the third measurement position (30°). The color bar indicates the conductivity scale.

The four groups of conductivity values are the reconstructed results of the same field but from different measurement positions. The complementary information from the four different measurement positions will increase the reliability of the result. Merging the conductivity values of the four coarse meshes into four fine meshes will strengthen the common knowledge and reduce the disagreements (for example the mesh and the noise). The mapping algorithm is:

$$\sigma^p_{fine\_n}\left(i^p\right) = \sum_{p=1}^{P} \sigma^p_{coarse\_n}\left(j^p\right) / P \qquad (7)$$

where P is the number of the measurement positions, i^p indicates the *i*th element of the *p*th 3D fine mesh, j^p indicates the *i*th element of the *p*th 3D coarse mesh, $\sigma^p_{fine\_n}$ and $\sigma^p_{coarse\_n}$ denote the conductivity values from the *n*th iteration, of the *p*th 3D fine and coarse mesh respectively. If $[x_i, y_i, z_i]$ indicates the coordinate of the center of i^p, $e^p_{coarse}(k)$ indicates the space of the *k*th element of the *p*th coarse mesh,

$$j^p = k \quad if \ [x_i, y_i, z_i] \in e^p_{coarse}(k) \qquad (8)$$

By using the mapping algorithm (7), the conductivity values of the four fine meshes are obtained. The cross-sectional images of the first fine mesh at 0° and the third fine mesh at 30° are shown in Figure 10. Although there are 6 layers in the 3D fine meshes, we only display 3 image layers by combining the two neighboring layers into one, corresponding to the layers of the coarse mesh. For iterations, knowing the reconstructed conductivity values of the fine

meshes, four groups of the predicted voltage measurements V_1^1, V_1^2, V_1^3 and V_1^4 can be computed, where 1 in the subscript indicates the first iteration, 1-4 in the superscript indicate the indexes of the measurement positions. By comparing the real measurement with the updated reference measurements, we can update the conductivity values until they converge. Then we can make the conductivity values of the four 3D fine meshes into one 3D picture or several cross-sectional pictures. The value of each pixel is

$$I(x,y,z)=\sum_{p=1}^{P}\sigma_{fine\_n}^{p}\left(h^{p}\right)\Big/P \tag{9}$$

where $I(x,y,z)$ indicates the conductivity value of the 3D space in the breast container, P denotes the number of the measurement positions, h^p denotes the *h*th element of the *p*th 3D fine mesh, $\sigma_{fine\_n}^{p}$ denotes the reconstructed conductivity value of the *p*th 3D fine mesh of the *n*th iteration. If $e_{fine}^{p}(K)$ denotes the space of the *K*th element of the *p*th fine mesh,

$$h^{p}=K \quad if \quad (x,y,z)\in e_{fine}^{p}(K) \tag{10}$$

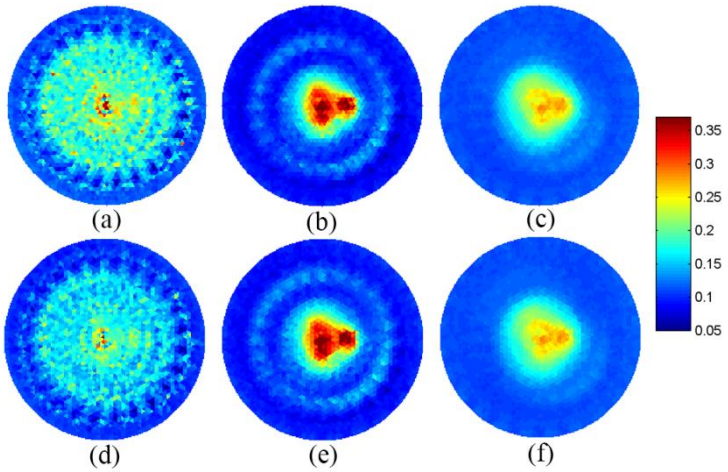

Figure 10. The conductivity values of the fine meshes at measurement position 0° and 30°. (a) to (c) show the conductivity of the 3D fine mesh at 0. (d) to (f) show the conductivity of the 3D fine mesh at 30°. The color bar indicates the conductivity scale.

Figure 11 shows the final cross-sectional images, which is contributed by the conductivity values of the four 3D fine meshes of the second iteration. The number of the pixels is 201×201. The big bright circular area in the first cross-sectional image is caused by the highly conductive skin. The bright area in the center of the second cross-sectional image is the image of the gland area. Before analyzing the second cross-sectional image, let's refer to the breast phantom in Figure 4 (a) and the discretized breast model in Figure 6 (b) and (e) to get the features of the breast: the ducts and acinus distribute similarly to an ellipse with two ends pointing to 11 and 6 O'clock. The red area in the center of Figure 11 (b) is consistent with these features, which indicates the cluster of the ducts and acinus. The darkest area in the center is caused by the nipple and the ducts, which converge to the nipple. The darkest area at 3 O'clock indicates that the tumor is present. The bright ring round the grand area is caused by the highly conductive skin. The dark area in between the gland area and the skin is the adipose tissue. In the third cross-sectional image, the gland area is clearly imaged in the center; the red area at 3 O'clock is a projection of the tumor, which is inevitable for planar electrode array (Bouchette et al., 2014);

the ducts and the acinus are not well imaged, as they are far from the electrodes. The data volume of the EIT problem is determined by the mesh. To make this program work, it requires at least 16G RAM. The computational time of the EIT problem is affected by the meshes, the algorithms and the number of measurement positions. The computational time is almost linear with the number of measurements positions. In this simulation, using an i7-4790 CPU @ 3.60 GHz, the computational time is about 93 seconds for one measurement position and about 374 seconds for 4 measurement positions.

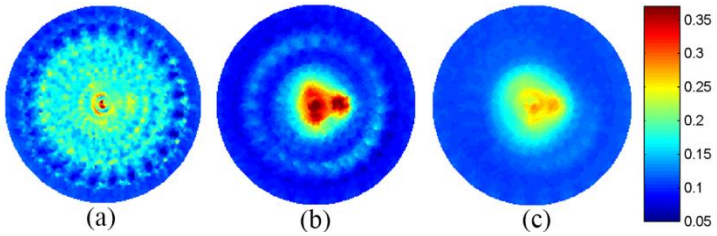

Figure 11. The final reconstructed conductivity distribution of four measurement positions. (a) to (c) indicate the cross-sectional images at the bottom, middle and top of the tank .

3. Result

3.1 Evaluation method

To evaluate the performance of an EIT system, we compare the geometric parameters of the target object and its image, which include the location parameters (the center of the tumor) and the shape parameters (the length and the width of the tumor). In this breast phantom, the target object is the tumor, which is defined as an ellipsoid and satisfies

$$\frac{(x-x_0)}{a^2}+\frac{(y-y_0)}{b^2}+\frac{z-z_0}{c^2}\le 1 \qquad (11)$$

where $[x_0, y_0, z_0]$ is the center of the ellipsoid, which is [2.5, 0, 1.5] (cm). *a*, *b* and *c* are the semi-principal axes of the ellipsoid, which is [1, 0.75, 0.5] (cm). Comparing $[x_0, y_0, z_0]$, *a*, and *b* between the real object and its image will give an objective analysis of the image accuracy. We name this quantitative evaluation method as image processing based error analysis method. The procedure is as follows. Firstly, estimate the vertical position of the object of interest by comparing the image contrast of each layer. Assume that the center of the object is located in the layer with the greatest image contrast, named the layer of interest (LOI). Secondly, convert the RGB image of the LOI to a binary image, and then extract the edge of the tumor. Finally, do curve fitting on the edge to find the parameters we need and compare the parameters with the standard object geometry to assess the accuracy of the result.

The image contrast of each layer is computed using the following equation.

$$c=\frac{\bar{I}_{Obj}}{\bar{I}_{Bg}} \qquad (12)$$

where $\bar{I}_{Obj}$ is the average of I greater than a threshold T, $\bar{I}_{Bg}$ is the average of I smaller than the threshold T. In this case, T is the conductivity value at half maximum of the conductivity range.

$$T = \min\left(I_{Layer}\right) + \frac{1}{2}\left[\max\left(I_{Layer}\right) - \min\left(I_{Layer}\right)\right] \quad (13)$$

where I_{Layer} denotes the conductivity values of an image layer. For Figure 11, Layer 2 is the LOI, that is: the most likely object layer. Converting the RGB image of the LOI to a binary image, we get a logical matrix containing ones where the object is and zeroes elsewhere:

$$I_B = \begin{cases} 0 & I_{Layer} \le T \\ 1 & I_{Layer} > T \end{cases} \quad (14)$$

where I_B is the image intensity. Following this, edge extraction is used to locate the coordinates of the pixels on the edge of the object. Assume that $[x_E, y_E]$ are the coordinates on the edge, where $x_E = [x_{E1}, x_{E2}, \cdots, x_{EN}]$, $y_E = [y_{E1}, y_{E2}, \cdots, y_{EN}]$, N represents the number of the coordinates. The center of the object $(\tilde{x}_0, \tilde{y}_0)$ can be estimated using (15).

$$\begin{cases} \tilde{x}_0 = \sum_{i=1}^{N} x_{Ei} / N \\ \tilde{y}_0 = \sum_{i=1}^{N} y_{Ei} / N \end{cases} \quad (15)$$

The size parameters can be computed by nonlinear least-squares curve fitting. For an elliptical object,

$$\left[\tilde{a}, \tilde{b}\right] = \arg\min_{\tilde{a},\tilde{b}} \left\| 1 - \frac{(x_E - \tilde{x}_0)^2}{\tilde{a}^2} - \frac{(y_E - \tilde{y}_0)^2}{\tilde{b}^2} \right\|_2^2 \quad (16)$$

where: $\arg\min_{\tilde{a},\tilde{b}}$ means the argument $\tilde{a}$ and $\tilde{b}$, which minimize what follows, $\| \ \|_2$ is the 2-norm, $\tilde{a}$ and $\tilde{b}$ indicates the computed semi-principal axes of the ellipse. We also define a parameter D to evaluate the whole distortion of the object.

$$D = \frac{\left\| 1 - \frac{(x_E - x_0)^2}{a^2} - \frac{(y_E - y_0)^2}{b^2} \right\|_2^2}{N} \quad (17)$$

where: x_0, y_0, a, b are the parameters of the real model. A small D value means a small difference between the image and the real object. If there is more than one object in the same layer, the total distortion is

$$D_{total} = \frac{\sum_{i=1}^{Num} \left\| 1 - \frac{\left(x_E^i - x_0^i\right)^2}{{a^i}^2} - \frac{\left(y_E^i - y_0^i\right)^2}{{b^i}^2} \right\|_2^2}{N} \quad (18)$$

where: *Num* indicates the number of objects. x_E^i and y_E^i indicates the coordinates of the points on the edge of the *i*th object; $\left(x_0^i, y_0^i\right)$ indicates the center of the *i*th object, a^i and b^i indicate the size of the *i*th object; *N* is the total number of points on the edges of the *N* objects.

3.2 The accuracy of the RPEIM system

Although the increase of measurement positions will benefit the image accuracy, they don't have linear relationship with image quality; or in other words, there will be no obvious improvement of image accuracy, where the number of rotations is greater than an optimum value. Figure 12 and Figure 13 present the reconstructed conductivity distributions of the breast phantom detected by the MK4 system and the RPEIM system with 8 measurement positions. According to Figure 11, Figure 12 and Figure 13, the RPEIM system gives a significant improvement in image accuracy over the MK4 system; however for the RPEIM system, the result from eight measurement positions doesn't show obvious improvement over the result from four measurement positions. Therefore the number of measurement positions for the RPEIM system is a non-linear optimization problem, which trades off the image accuracy and the computational time. Figure 14 shows the edges of the tumor corresponding to different numbers of measurement positions. By using the image processing based error analysis method, we get the position and shape parameters of the tumor, which are tabulated in Table 1 and plotted in Figure 15, this explores the relationship between the number of rotations and the physical location errors of the tumor.

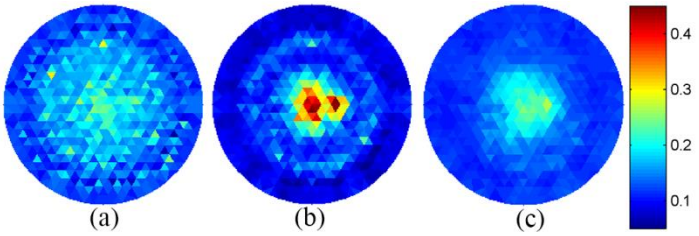

Figure 12. The reconstructed conductivity maps of the digital breast phantom using the MK4 system

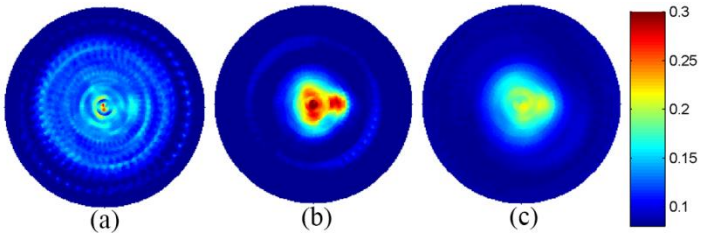

Figure 13. The reconstructed conductivity maps of the digital breast phantom using the RPEIM system with 8 measurement positions

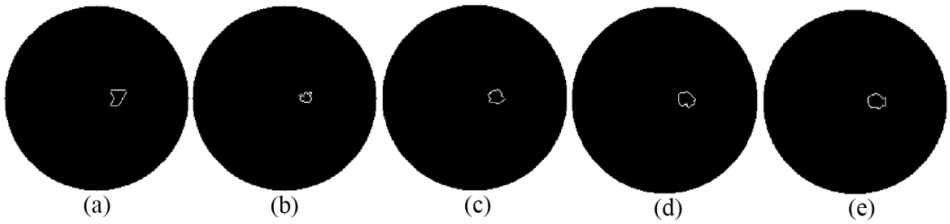

Figure 14. The edge of the tumor corresponds to different numbers of measurement positions. (a) is from the MK4 system. (b) to (f) are from the RPEIM system using 2, 3, 4 and 8 measurement positions.

In Figure 14, the shape of the tumor from the MK4 system is seriously affected by the

triangular shape of the elements; however as the number of the measurement positions increases, the shape accuracy of the tumor is significantly improved. Table 1 and Figure 15 present the critical parameters of the image and give a quantitative analysis of the relationship between the image accuracy and the number of measurement positions. According to Table 1 and Figure 15 (a), the image contrast drops from 10.27 for the MK4 system to 5.85 for the RPEIM system with 5 measurement positions and then becomes stable. In image reconstructions, because of the ill-posed nature and the influence of the noise, there will be some mesh elements having abnormally high or low conductivity values, which results in a big image contrast for the MK4 system; however when we have several measurement positions and use the merged value to denote the conductivity value at $[x, y, z]$, the abnormally high or low values will be averaged, resulting in a reduced image contrast. The image contrast doesn't drop linearly with the number of measurement positions; it becomes stable when the number of measurement positions exceeding a threshold value, which is 5 in this case. The image distortion D gives a comprehensive evaluation of the image accuracy of the tumor, including the location and the shape of the tumor. In Figure 15 (a), the curve of the image distortion (D) drops sharply from 1 to 4 measurement positions and becomes stable from 4 to 7 measurement positions and then slightly rises at 8 measurements positions. This indicates that there is a significant improvement of image accuracy as the number of measurement positions increases from 1 to 4, after which the improvement becomes very marginal. The center shift is the distance between the centers of the real object and its image, which assesses the positional accuracy. According to Figure 15 (b), the positional error doesn't get smaller as the number of measurement positions increases. The errors of the object length and width in Figure 15 (b) are used to assess the size error of the tumor. As the number of measurement positions increases to 3, the size error stabilizes. By comprehensively analyzing the reconstructed conductivity distributions, the outlines of the tumor in Figure 14 and the critical parameters in Table 1 and Figure 15, and also considering the computational time, we suggest three to five measurement positions for a real experiment. Three measurement positions is preferred to reduce computational time, whilst five measurement positions will give higher accuracy.

Table 1. The critical parameters obtained from the images

Parameters	MK4	The RPEIM system		
Measurement positions	1	2	3	4
Horizontal center, (cm)	[2.06,0.11]	[2.13,0.11]	[2.07,0.08]	[2.10,0.10]
Vertical center in layer	Layer 2	Layer 2	Layer 2	Layer 2
Conductivity contrast in LOI	10.27	8.19	6.71	7.66
Half length and width, [a b](cm)	[0.78, 0.86]	[0.59, 0.50]	[0.81, 0.68]	[0.81, 0.70]
Object distortion, D	0.38	0.30	0.30	0.26
Parameters	The RPEIM system			
Measurement positions	5	6	7	8
Horizontal center, (cm)	[2.12, 0.11]	[2.10, 0.07]	[2.07, 0.09]	[2.10, 0.07]
Vertical center in layer	Layer 2	Layer 2	Layer 2	Layer 2
Conductivity contrast in LOI	5.85	5.69	5.67	6.42
Half length and width, [a b](cm)	[0.76, 0.71]	[0.82, 0.73]	[0.70, 0.63]	[0.9, 0.7]
Object distortion, D	0.26	0.27	0.25	0.29

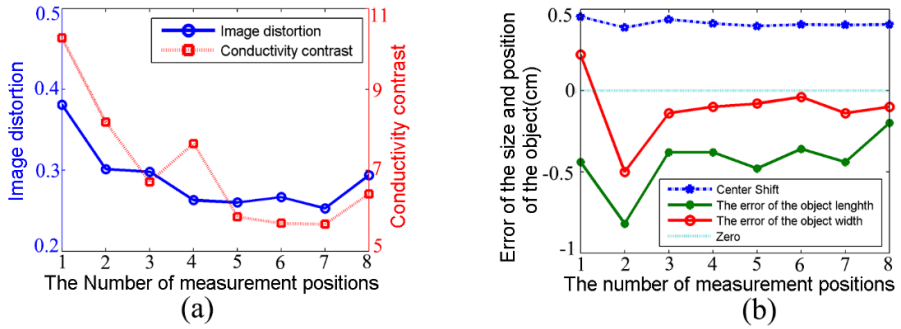

Figure 15. Relationship between the image quality and the number of measurement positions. (a) shows the conductivity contrast and the object distortion versus the number of measurement positions. (b) presents the size and the position errors of the object versus the number of measurement

3.3 The Spatial Resolution of the RPEIM System

A breast phantom with two tumors in Figure 16 is used to illustrate the advantage of the RPEIM system in spatial resolution. The two tumors are the same size with length of 2 cm, width of 1.5 cm, and height of 1 cm, but they are placed perpendicularly. Tumor 1 is placed at [2.5, 1.25, 1.5] (cm); Tumor 2 is placed at [2.5, -1.5, 1.5] (cm). The smallest boundary to boundary distance between the two tumors is 1 cm. The spatial resolution of a EIT system is considered relative to the electrode density and the distance to the electrode array (Hartov et al., 2005). According to the electrode arrangement of the MK4 and RPEIM system, it can at least distinguish the two objects at the electrode-contact plane with a separation distance of about 1.7 cm. In this case, we aim to show the improvement in spatial resolution using the RPEIM system, by separating the two objects with a distance smaller the adjacent electrode distance.

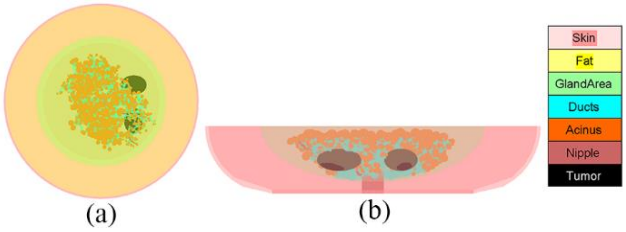

Figure 16. The breast model with two tumors. (a) is the XY view. (b) is the YZ view

Figure 17 and Figure 18 present the reconstructed image from the MK4 system and the RPEIM system with five measurement positions respectively. Clearly Figure 18 is much closer to the digital breast phantom than Figure 17. For the case with two tumors, we use two steps to assess the image accuracy: general analysis which analyzes the image as a whole and further analysis which analyzes the region of interest (ROI). Step 1: roughly establishes the location and size parameters of the two tumors from Figure 18 (b), using the image processing based error analysis method. When two (or more) tumors are close together in the breast, one will affect the reconstructed conductivity of another and its surrounding area, especially for the region in between them. In this situation, using the threshold at half maximum of the conductivity range may be inappropriate. The threshold in this case is 0.25

S/m, which is a minimal value that separates the images of the two tumor. The roughly analyzed geometrical parameters of the two tumors are shown in Table 2. The center of Tumor 1 and Tumor 2 shift 0.65 cm and 0.48 cm respectively. The object distortion of Tumor 1 and Tumor 2 are 0.92 and 0.34 respectively. The image of Tumor 2 is more accurate than Tumor 1. This may be because Tumor 1 is closer to the region of the high density gland than Tumor 2 and the signal from the high density gland is so strong that it affects the detection of the tumor nearby. Step 2: use the location of Tumor 2 as a reference (as the location of Tumor 2 is more accurate) and plot the conductivity distributions in Figure 19 (b) and (d), along the black lines in Figure 19 (a) and (c), to provide further analysis to the ROI. Both Figure 19 (b) and (d) have two peaks; however the curve in Figure 19 (b) is too coarse to evaluate the locations and the sizes of the two tumors. While Figure 19 (d) shows two clearly separated humps with a boundary-to-boundary distance of 0.99 cm, which is consistent to the breast model. Please note the difference from Step 1, in which we used one threshold to determine the sizes and locations of the tumors, in Step 2, we use two thresholds as the conductivity scales of the two tumors are different in Figure 19 (d). If we take the inflection points at the ends of the two humps as the boundary of the two tumors, the sizes of the two tumors along y-axis are 1.22 cm and 1.04 cm. If we assume that the centers of the two tumors are at the middle of the two humps, the coordinates of the tumors' centers on the y-axis are 0.88 cm and -1.24 cm. By observing the cross-sectional images in Figure 17 and the conductivity distribution of the ROI in Figure 19 (b), we find that when the boundary-to-boundary distance of the two tumors are equal to 1cm, it is difficult for the MK4 system to separate the two tumors and get accurate positions for them. However by observing Figure 18 and Figure 19 (d), we conclude that 1) the RPEIM system can separate the two tumors with a boundary-to-boundary distance equal to 1 cm; 2) the RPEIM system can provide a better spatial resolution than the MK4 system.

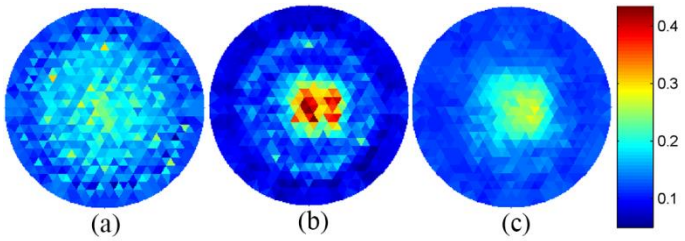

Figure 17. The reconstructed result of the two-tumor breast phantom using the MK4 system. (a) to (c) indicate the cross-sectional images from the bottom to the top.

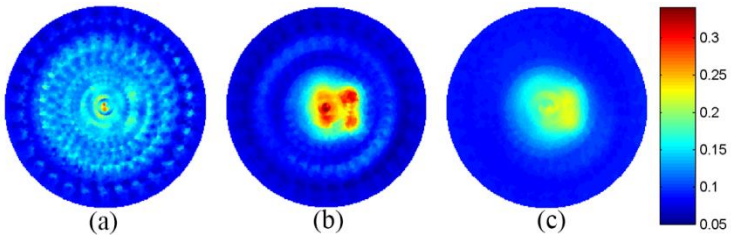

Figure 18. The reconstructed result of the two-tumor breast phantom using the RPEIM system with 5 measurement positions. (a) to (c) indicate the cross-sectional images from the bottom to the top.

Table 2. The roughly estimated parameters of the two tumours (Step 1)

Tumour 1			
Parameters	Real value	Estimated value	Error
Horizontal centre (cm)	[2.5,1.25]	[1.98,0.86]	[-0.52,-0.39]
Vertical centre	Layer 2	Layer 2	
Length and width (cm)	[2,1.5]	[1.80,1.38]	[-0.2,-0.12]
Centre shift (cm)	0.65		
Object distortion	0.92		
Tumour 2			
Parameters	Real Value	Estimated value	Error
Horizontal centre (cm)	[2.5,-1.5]	[2.18,-1.14]	[-0.32,0.36]
Vertical centre	Layer 2	Layer 2	
Length and width (cm)	[1.5,2]	[1.08,1.38]	[-0.42,-0.62]
Centre shift (cm)	0.48		
Object distortion	0.34		
Total distortion of the two tumors	0.64		

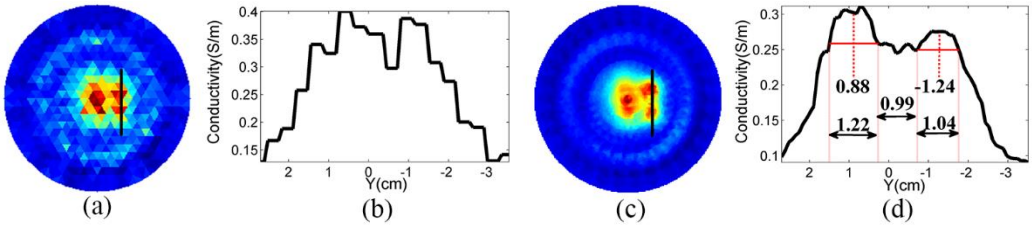

Figure 19. The conductivity distribution of the ROI. (b) and (d) plot the conductivity distribution of the region on the black lines in (a) and (c). (a) and (c) are the images from Figure 17 (b) and Figure 18 (b) respectively. (d) shows the further analyzed parameters from Step 2.

3.4 The Noise tolerance of the RPEIM system

The conductivity value, from the RPEIM system using the synchronous mesh method, is a merged value from multiple measurement positions; therefore it is supposed to have a better noise tolerance. To prove this point, we still use the breast model in Figure 4. We add 30 dB white Gaussian noise and $\pm 1\%$ random multiplicative noise to the simulated measurements at the 500 kHz operating frequency. For 1000 samples, the SNR of the whole system is approximately 45 dB. The reconstructed images corresponding to the MK4 system and the RPEIM system with four measurement positions are shown in Figure 20 and Figure 21. Comparing Figure 20 with Figure 12, which are all from the MK4 system but with different noise levels, the reconstructed result in Figure 20 is seriously affected by the noise. The red elements at 12 o'clock to 6 o'clock indicate the presence of the cluster of the ducts and acinus, but obviously the distribution is inconsistent with the breast phantom. The highly conductive elements at 3 o'clock indicate the presence of the tumor. By comparing Figure 11 and Figure 21, which are all from the RPEIM system with 4 measurement positions, we find that reducing the SNR from 70dB to 45 dB doesn't make a big change of the reconstructed result. The image of the tumor and the cluster of the ducts and acinus in Figure 21 is still clear and

consistent with the breast phantom. Comparing Figure 20 and Figure 21, which are from different systems but with the same noise level, we find that the conductivity distribution in Figure 21 from the RPEIM system is much closer to the breast phantom than that in Figure 20. Thus, we conclude that 1) for the same system but with different noise levels, the reconstructed result from the RPEIM system is not affected as badly as that from the MK4 system; 2) for the same noise level but different systems, the RPEIM system performs better than the MK4 system in image accuracy. These two points prove that the RPEIM system has a better noise tolerance than the MK4 system.

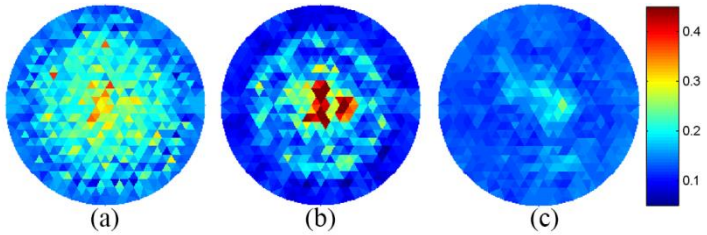

Figure 20. The reconstructed result from the MK4 system, with SNR of 45 dB. (a) to (c) indicate the cross-sectional images from the bottom to the top.

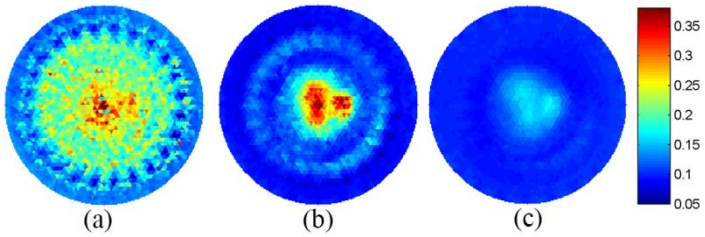

Figure 21. The reconstructed result from the RPEIM system of four measurement positions, with SNR of 45 dB. (a) to (c) indicate the cross-sectional images from the bottom to the top.

3.5 Simulations Based on a Real Patient

We reported the conductivity map of Patient 0703 detected by the MK4 system and gave detailed analysis in reference (Zhang et al., 2014d). In this section, we set up a digital breast phantom of Patient 0703 and apply this breast phantom to both the MK4 system and the RPEIM system to achieve two comparisons: 1) we compare the conductivity maps of the real patient and the breast phantom, which will demonstrate that the digital breast phantom is a good replica of the breast of Patient 0703; 2) we compare the conductivity maps from the MK4 system and the RPEIM system based on the breast phantom, which will present the improvements of the RPEIM system. Although this study is based on simulation, this approach will make sure that the mock clinical trial is very close to realistic.

Figure 22 shows the X-ray images and the conductivity maps of Patient 0703's left breast, in which LMLO and LCC indicate the mediolateral-oblique (MLO) and craniocaudal (CC) view of the left breast (the first L indicates the left breast). For detailed information of using the MK4 system to examine Patient 0703, please refer to reference (Zhang et al., 2014d). The breast phantom of Patient 0703 is set up according to both the X-ray images and the conductivity maps. Before setting up the breast phantom, it should be emphasized that the

breast phantom cannot be exactly the same as the real breast as the inner structure and the exact conductivity values of the breast tissues are unknown, but the breast phantom can be close to the real breast, if it is carefully defined according to the features of the real breast. The cup size of Patient 0703 is C. In examination, the thickness of the breast is pressed to 1.8cm by the MK4 system. The features of the breast of Patient 0703 are: 1) according to Figure 22 (a), the mammary gland in the caudal breast is denser than the cranial breast, so for the breast phantom, there should be more ducts and acinus in the caudal breast than the cranial breast (Figure 23 (b)); 2) according to Figure 22 (b), the mammary gland on the left hand side is dense and has a round profile; however the mammary gland on the right hand side is not dense and has an almost straight profile, so the breast phantom is built as Figure 23 (c); 3) according to Figure 22 (c) and (d), the tumor is at the upper outside quadrant; 4) according to Figure 22 (c), the conductivity in the upper inner quadrant (UIQ) is relatively small, so there should be less ducts and acinus in that area. With these features, we set up the breast phantom of Patient 0703 in Figure 23. The size and location of the tumor is estimated according to the conductivity maps, which is located at [-2.98 1.47 0.9] (cm) and has a size of 0.7 cm in width, 1.3 cm in length and 0.5 cm in height. The conductivity values of the breast phantom are estimated according to the conductivity maps and shown in Table 3. In simulations, the operating frequency is 500 kHz, the sampling frequency is 20 MSa/s, the sample number is 1000, the ADCs are 14 bit, the background noise is 60dB white Gaussian noise, and the multiplicative noise is $\pm 0.5\%$ random noise.

Figure 24 presents the simulated result of the breast phantom detected by the MK4 system. The red elements highlighted by the circles indicate the presence of the tumor. The red area in the center is caused by the gland. By comparing Figure 22 (c) (d) and Figure 24, we find that 1) the size and the location of the tumor in Figure 22 (c) (d) and Figure 24 are similar; 2) the areas of the gland (the red area in the center of the conductivity maps) in Figure 22 (c) (d) and Figure 24 are similar; 3) both Figure 22 (c) and Figure 24 (a) have a less conductive area in the UIQ and the shapes of the less conductive areas are similar; therefore we conclude that 1) the breast phantom could simulate the conductivity distribution of a real breast at the precision that the EIT systems can distinguish; 2) the digital breast phantom is valuable for the mock clinical trials of EIT. Knowing that the breast phantom of Patient 0703 could contribute to a similar conductivity map with the real examination, we apply the RPEIM system to this breast phantom for a mock clinical trial. Figure 25 shows the reconstructed conductivity maps of the breast phantom, detected by the RPEIM system with five measurement positions. Comparing Figure 24 and Figure 25, we find that the result from the MK4 system is seriously affected by the noise and the size of the mesh elements; however by using the RPEIM system, the influences from the noise and the size of the mesh are significantly reduced, the image of the tumor is much clearer, and the spatial resolution of the conductivity maps is significantly improved.

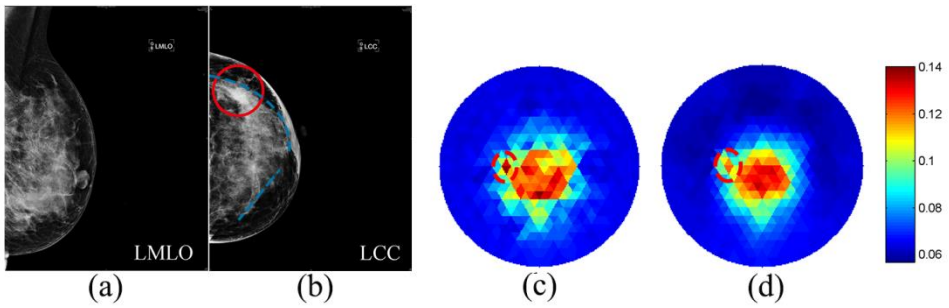

Figure 22. X-ray images and conductivity maps of Patient 0703, tumor indicated by red circle. (a) and (b) are the LMLO and the LCC image. (c) and (d) are the conductivity maps of the bottom and the top layer.

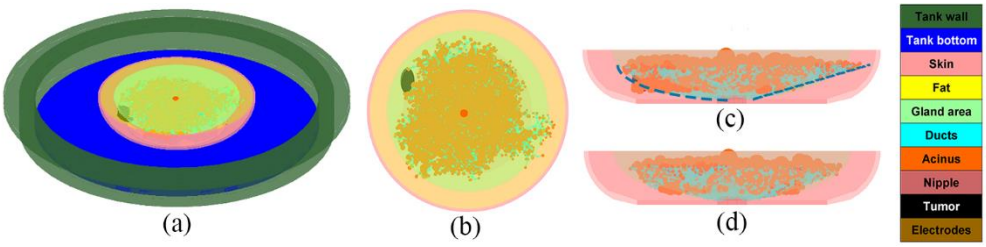

Figure 23. The breast phantom of Patient 0703. (a) shows the compressed breast in the breast container. (b) is the XY view of the breast phantom. (c) is the XZ view of the breast phantom. (d) is the YZ view of the breast phantom.

Table 3. The conductivity of the breast phantom

Breast	Saline	Skin	Fat	Gland area	Nipple, ducts, acinus	Tumor
Conductivity (S/m)	0.05	0.15	0.04	0.06	0.14	0.6

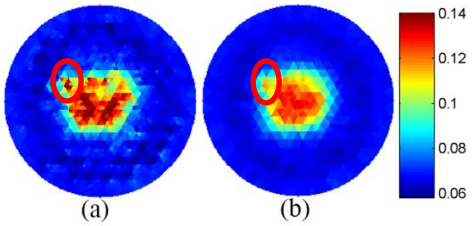

Figure 24. The conductivity distribution of the breast phantom of Patient 0703 detected by the MK4 system.

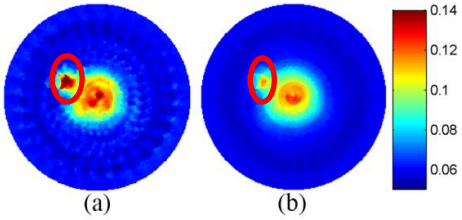

Figure 25. The conductivity distribution of the breast phantom of Patient 0703 detected by the RPEIM system with 5 measurement positions, using two layers.

4. Discussion

The advantages of the RPEIM system compared with the former MK4 system are: high accuracy, high spatial resolution and good tolerance to noise.

Regarding the accuracy, to make a reliable performance assessment of the RPEIM system, we define some critical parameters, which include: conductivity contrast, object center, object size (length and width), errors of object center and size, and object distortion. These parameters are plotted and tabulated in Figure 15 and Table 1 to investigate the relationships between the image accuracy and the number of measurement positions.

Generally the RPEIM system generates better results than the MK4 system. For the RPEIM system, we suggest three to five measurement positions: three measurement positions is preferred for speed; five measurement positions is preferred for higher accuracy. Increasing the number of measurement positions beyond 5 is pointless, as it is time consuming and no further improvement can be obtained.

As for the spatial resolution, the RPEIM system exhibits a significant improvement over the MK4 system. To demonstrate this, a breast model with two tumors is employed and the results corresponding to the MK4 system and the RPEIM system with 5 measurement positions are shown in Figure 17, Figure 18 and Figure 19. For the MK4 system, the image of the normal gland and the images of the two tumors are mixed together. If we didn't have the knowledge of the structures of the breast phantom, we could hardly determine the existence of the tumors. However for the RPEIM system, the images of the normal gland and the two tumors are clearly separated. By plotting the conductivity distribution across the centers of the two tumors in Figure 19 (d), we estimated that the boundary to boundary distance is equal to 0.99 cm. This result is very close to the real distance of 1cm. Thus, we believe that the RPEIM system could deliver a better spatial resolution than the MK4 system.

Considering noise, the RPEIM system has a much better noise tolerance than the MK4 system as the errors of the reconstructed conductivity values are averaged by the algorithm of the synchronous mesh method. Figure 12 and Figure 20 present the reconstructed results of the breast model in Figure 4, by using 70 dB and 45 dB measurements from the MK4 system. Comparing these two results, we can find that as the noise increases, the image quality deteriorates seriously. Figure 11 and Figure 21 present the reconstructed results of the same breast model, by using 70 dB and 45 dB measurements from the RPEIM system with four measurement positions. According to these results, we can find that although the noise increased to a high level, it didn't affect the detection of the tumor, which proves that the RPEIM system could achieve a good noise tolerance by increasing the number of the measurement positions. By comparing Figure 20 and Figure 21, we believe that the RPEIM system with the synchronous mesh method not only reduces the errors caused by the noise from the system, but also reduces the errors caused by the size of the mesh elements.

To validate our study, we made simulations based on Patient 0703, whose tumor was detected by the MK4 system. To apply the RPEIM system to this patient, we firstly built a digital breast phantom in Figure 23. By comparing the simulated result in Figure 24 with the experimental result in Figure 22, we conclude that 1) the digital breast phantom is a close replica of the real breast; 2) the digital breast phantom could be an alternative approach to clinical trials when the number of volunteers is limited. We then applied the RPEIM system to this digital breast phantom. By comparing the result in Figure 25 with the results in Figure 22 and Figure 24, we conclude that the RPEIM system has better performances in image accuracy, spatial resolution and noise tolerance than the MK4 system.

5. Conclusion and future work

The RPEIM system is superior to the MK4 system in image accuracy, spatial resolution and noise tolerance due to the increase in the number of independent measurements and the synchronous mesh method. The increase of the independent measurements provides more

boundary conditions, which increases the solution constraints, hence ensuring a more accurate result. The synchronous mesh method avoids refining the mesh to support the electrode rotations; therefore it prevents greater ill-conditioning caused by the fine mesh. The rotations of the mesh, together with the electrode array, permit the conductivity maps to be reconstructed at different angles. The mapping algorithm merges the conductivity values of the coarse meshes into the values of the fine meshes, and finally combines them into one 3D image or several cross-sectional images. This minimizes the influence of the mesh and makes the conductivity distribution smooth, not lumpy, hence giving better spatial resolution. The final image is reconstructed from several groups of measurements; therefore the random noise from one group of measurements will be ameliorated, hence delivering better noise tolerance. In general, the RPEIM system with the synchronous mesh benefits the image accuracy, spatial resolution and noise tolerance. However the improvement of the image quality is not linear with the number of measurement positions. There won't be an obvious improvement if the number of measurement positions exceeds five. Indeed, considering the computational time, three to five positions are reasonable in practice. A digital breast model applicable to EIT is proposed in this paper. This is valuable in the mock clinical situation as it provides unlimited data for EIM assessment and helps to set the tumor detection requirements for a particular EIM system (for example the detectable tumor size, depth, and the conductivity contrast between the tumor and the surrounding normal tissue). We have done some work on the improvement of image accuracy, spatial resolution and noise tolerance. In the future, we will consider the difficulties of the planar electrode array in detecting the tumor in remote regions, and work on the improvement of the sensitivity in depth.

REFERENCES

BABAEIZADEH, S., BROOKS, D. H., ISAACSON, D. & NEWELL, J. C. 2006. Electrode boundary conditions and experimental validation for BEM-based EIT forward and inverse solutions. *Ieee Transactions on Medical Imaging,* 25**,** 1180-1188.

BARBER, D. C. 2005. EIT: The view from sheffield. *In:* HOLDER, D. S. (ed.) *Electrical impedance tomography : methods, history and applications.* Bristol: Institute of Physics.

BOUCHETTE, G., CHURCH, P., MCFEE, J. E. & ADLER, A. 2014. Imaging of Compact Objects Buried in Underwater Sediments Using Electrical Impedance Tomography. *Geoscience and Remote Sensing, IEEE Transactions on,* 52**,** 1407-1417.

CAMPBELL, A. M. & LAND, D. V. 1992. Dielectric properties of female human breast tissue measured in vitro at 3.2 GHz. *Physics in Medicine and Biology,* 37**,** 193.

DÄHNERT, W. 2007. Breast. *Radiology review manual.* 6th ed. Philadelphia: Lippincott Williams Wilkins.

DE LUCIA, M., PARKER, G. J. M., EMBLETON, K., NEWTON, J. M. & WALSH, V. 2007. Diffusion tensor MRI-based estimation of the influence of brain tissue anisotropy on the effects of transcranial magnetic stimulation. *Neuroimage,* 36**,** 1159-1170.

DONG, G. Y., ZOU, J., BAYFORD, R. H., MA, X. S., GAO, S. K., YAN, W. & GE, M. L. 2005. The comparison between FVM and FEM for EIT forward problem. *Ieee Transactions on Magnetics,* 41**,** 1468-1471.

FROUNCHI, J. & BAZZAZI, A. 2003. High resolution rotary capacitance tomography system. *3rd World Congress on IPT Banff.* Canada.

GAGNON, H., COUSINEAU, M., ADLER, A. & HARTINGER, A. E. 2010. A resistive mesh phantom for assessing the performance of EIT systems. *IEEE Trans Biomed Eng,* 57**,** 2257-66.

GISSER, D. G., ISAACSON, D. & NEWELL, J. C. 1990. Electric Current Computed Tomography and Eigenvalues. *SIAM Journal on Applied Mathematics,* 50**,** 1623-1634.

GUOFENG, Q., WEI, W., WEI, D., FAN, Z., SINCLAIR, A. J. & CHATWIN, C. R. 2012. Bioimpedance analysis for the characterization of breast cancer cells in suspension. *IEEE Trans Biomed Eng,* 59**,** 2321-9.

HANSEN, P. C. & OLEARY, D. P. 1993. The Use of the L-Curve in the Regularization of Discrete Iii-Posed Problems. *Siam Journal on Scientific Computing,* 14**,** 1487-1503.

HARTOV, A., SONI, N. & HALTER, R. 2005. Breast cancer screening with elecrical impedance tomography. *In:* HOLDER, D. S. (ed.) *Electrical impedance tomography : methods, history and applications.* Bristol: Institute of Physics.

HASSAN, A. M. & EL-SHENAWEE, M. 2011. Review of electromagnetic techniques for breast cancer detection. *IEEE Rev Biomed Eng,* 4**,** 103-18.

HOLDER, D. S., HANQUAN, Y. & RAO, A. 1996. Some practical biological phantoms for calibrating multifrequency electrical impedance tomography. *Physiological Measurement,* 17**,** A167.

HUANG, C.-N., YU, F.-M. & CHUNG, H.-Y. 2007. Rotational electrical impedance tomography. *Measurement Science and Technology,* 18**,** 2958.

HUSSAIN, M., RYNN, L., RIORDAN, C. & REGAN, P. J. 2003. Nipple-areola reconstruction: outcome assessment. *European Journal of Plastic Surgery,* 26**,** 356-358.

JOSSINET, J. 1996. Variability of impedivity in normal and pathological breast tissue. *Med Biol Eng Comput,* 34**,** 346-50.

JOSSINET, J. 1998. The impedivity of freshly excised human breast tissue. *Physiol Meas,* 19**,** 61-75.

KAUFMAN, L. & NEUMAIER, A. 1996. PET regularization by envelope guided conjugate gradients. *Ieee Transactions on Medical Imaging,* 15**,** 385-389.

LAVARELLO, R., KAMALABADI, F. & O'BRIEN, W. D. 2006. A regularized inverse approach to ultrasonic pulse-echo imaging. *Ieee Transactions on Medical Imaging,* 25**,** 712-722.

LAZEBNIK, M., POPOVIC, D., MCCARTNEY, L., WATKINS, C. B., LINDSTROM, M. J., HARTER, J., SEWALL, S., OGILVIE, T., MAGLIOCCO, A., BRESLIN, T. M., TEMPLE, W., MEW, D., BOOSKE, J. H., OKONIEWSKI, M. & HAGNESS, S. C. 2007. A large-scale study of the ultrawideband microwave dielectric properties of normal, benign and malignant breast tissues obtained from cancer surgeries. *Phys Med Biol,* 52**,** 6093-115.

MURPHY, S. C. & YORK, T. A. 2006. Electrical impedance tomography with non-stationary electrodes. *Measurement Science and Technology,* 17**,** 3042.

SADLEIR, R. J., SAJIB, S. Z., KIM, H. J., KWON, O. I. & WOO, E. J. 2013. Simulations and phantom evaluations of magnetic resonance electrical impedance tomography (MREIT) for breast cancer detection. *J Magn Reson,* 230**,** 40-9.

SUROWIEC, A. J., STUCHLY, S. S., BARR, J. B. & SWARUP, A. 1988. Dielectric properties of breast carcinoma and the surrounding tissues. *IEEE Trans Biomed Eng,* 35**,** 257-63.

SUTRADHAR, A. & MILLER, M. J. 2013. In vivo measurement of breast skin elasticity and breast skin thickness. *Skin Res Technol,* 19**,** e191-9.

SZE, G. 2012. *Detection of breast cancer with electrical impedance mammography.* Doctoral thesis, University of Sussex.

TANG, M., WANG, W., WHEELER, J., MCCORMICK, M. & DONG, X. 2002. The number of electrodes and

basis functions in EIT image reconstruction. *Physiol Meas,* 23**,** 129-40.

THE BREAST ANATOMY. 2013. *Breast Anatomy* [Online]. Available: http://www.rcsed.ac.uk/fellows/aaasalem/BreastanatomyDr.htm [Accessed Nov 25 2013].

VOGEL, C. R. 1996. Non-convergence of the L-curve regularization parameter selection method. *Inverse Problems,* 12**,** 535-547.

XU, G. Z., WU, H. L., YANG, S., LIU, S., LI, Y., YANG, Q. X., YAN, W. L. & WANG, M. S. 2005. 3-D electrical impedance tomography forward problem with finite element method. *Ieee Transactions on Magnetics,* 41**,** 1832-1835.

YU, F. M., HUANG, C. N., CHANG, F. W. & CHUNG, H. Y. 2006. A Rotative Electrical Impedance Tomography Reconstruction System. *4th International Symposium on Instrumentation Science and Technology (ISIST' 2006),* 48.

ZHANG, X., CHATWIN, C. & WANG, W. 2014a. A Comparison of Two Image Reconstruction Methods Based on the Sussex MK4 System. *the 15th International Conference on Biomedical Applications of Electrical Impedance Tomography.* Canada.

ZHANG, X., QURESHI, T., CHATWIN, C. & WANG, W. 2014b. Validity of Using the Ratio Difference Algorithm Assumption for the Sussex EIT MK4 System. *the 15th International Conference on Biomedical Applications of Electrical Impedance Tomography.* Canada.

ZHANG, X., WANG, W. & CHATWIN, C. 2014c. The Data Acquisition Method of the Sussex MK4 EIT System. *15th International Conference on Biomedical Applications of Electrical Impedance Tomography.* Canada.

ZHANG, X., WANG, W., SZE, G., BARBER, D. & CHATWIN, C. 2014d. An Image Reconstruction Algorithm for 3-D Electrical Impedance Mammography. *Medical Imaging, IEEE Transactions on,* 33**,** 2223-2241.